Spatial distribution of the optogalvanic signal in a microplasma detector for lab-on-a-chip gas analysis

A Persson[1,2] and M Berglund[1,2]

[1]Department of Engineering Sciences, Ångström Space Technology Centre, Uppsala University, Uppsala, SE-75121, Sweden.

[2]Department of Engineering Sciences, Division of Microsystem Technology, Uppsala University, Uppsala, SE-751 21, Sweden.

E-mail: anders.persson@angstrom.uu.se

This document is the Post-print version of a Published Work that appeared in final form in Laser Physics Letters. It should be cited as "Anders Persson and Martin Berglund 2016 Laser Phys. Lett. 13 075703" (doi:10.1088/1612-2011/13/7/075703). To access the final edited and published work see: http://iopscience.iop.org/article/10.1088/1612-2011/13/7/075703

Abstract. Gas sensors are characterized by their sensitivity and selectivity, preferably combined with versatility, where the selectivity can be altered, without complex modifications and whiteout loosing sensitivity. If aimed at lab-on-a-chip applications, the sensor also must be able to analyze small samples. Today, sensors combining selectivity and versatility for chip-level gas analysis are scarce; however, this paper investigates how miniaturized optogalvanic spectroscopy can fill this gap. By studying the spatial distribution of the optogalvanic signal inside a microplasma, it is shown that the signal is generated in the miniscule gas volume of the sheath surrounding the plasma probe that collects it. Still, a strong and stable spectroscopic signal can be extracted from the sheath, and the sample concentrations can be calculated using straightforward plasma theory. The minimum detectable absorption and the noise equivalent absorption sensitivity of the system are estimated to be less than 1.4×10^{-9} $Hz^{-0.5}$ and 2.8×10^{-9} $cm^{-1}Hz^{-0.5}$, respectively, without cavity enhancement. Combined with inherited versatility from absorption spectroscopy and the capability of handling sub-nanogram samples, this makes optogalvanic spectrometry an excellent candidate for future lab-on-a-chip gas analyzers.

1. Introduction

Gas analysis in lab-on-a-chip (LOC) applications typically refers to the detection and quantification of one or several substances in a sample volume of a few tens of microliters. A sensor for such applications should combine ppm sensitivity, with high selectivity in order to enable analysis of complex gas mixtures. Form a technological point of view, the sensor should also be versatile, in order to enable easy modification of its selectivity to a new substance. However, most current LOC gas

sensors lack both versatility and selectivity, which often is compensated by employing gas chromatography. [1]

For macroscopic systems, on the other hand, different absorption spectroscopy methods, e.g., cavity enhanced absorption spectroscopy [2] (CEAS) and integrating cavity output spectroscopy [3] (ICOS), offer great selectivity and versatility, where only the wavelength of the laser that is used to probe the sample has to be changed in order to study a new substance. Today, lasers with wavelengths throughout the ultraviolet, visible and infrared (IR) spectra are commercially available, making absorption spectroscopy an important tool in such diverse fields as environmental sciences [4,5], biomedicine [6] and planetary exploration [7,8].

However, absorption spectroscopy is not well suited for LOC applications, since it is inherently difficult to miniaturize, and handles limited sample amounts poorly [9]. In most embodiments, the technique relies on a sample cell of sufficient volume and pressure to achieve proper detection – in high-end systems typically around a liter filled to 1-10 kPa [3,10,11] – and if any of these parameters are reduced, the sensitivity drops drastically. Moreover, increasing the pressure to compensate for a reduction in volume is not an option, since this would greatly reduce the selectivity via peak broadening, and still not enable the study of small samples.

An alternative to absorption spectroscopy is photoacoustic spectroscopy (PAS), in which the acoustic signal created by the absorption of a laser pulse in a gaseous sample is recorded by a sensitive microphone [12]. PAS commonly utilizes smaller sample cells but higher pressures, typically milliliters at 100 kPa.

Interesting in this respect is the somewhat derelict field of optogalvanic (OG) spectroscopy [13], which was a hot research topic in the 1970s and early 80s, but was more or less abandoned, since it did not find any lasting applications outside of science. This was mainly due to the lack of reliable light sources at the time, but when the development of tunable single-mode laser took off in the 1990s, they were not applied to OG spectroscopy, but rather to other absorption techniques, probably due to the parallel development of new absorption-detector materials. Still, at its peak, OG spectroscopy was often found to be more sensitive than both emission and absorption spectroscopy. [14,15]

Optogalvanic spectroscopy (OGS) relies on the OG effect that describes the perturbation of a gas discharge, or plasma, by light in resonance with transitions in the atoms or molecules that makes up the sample. This perturbation stems from photon-induced excitations that in one way or another affects the impedance of the plasma – a parameter that can be easily measured and translated into detailed information about the composition of the sample, given access to adequate theory. [13]

From a LOC point of view, one property of OG spectroscopy is of particular interest. Several authors have observed that the signal in an OG sensor stems from only a limited part of the plasma if it is measured by the means of a plasma probe [14–18]. Most reports identify the sheath of the probe as the key region for the signal generation, but no one has studied this phenomena in more than one dimension, and only Suszuki *et al* [15] have tried to develop theory to explain it. However, the ability to draw a strong spectroscopic signal from a very small gas volume suggests that OG spectroscopy may be well suited for miniaturization – something that the present study aims to verify.

By employing a microwave-induced microplasma source based on a stripline split-ring resonator (SSRR) [19], and equipping it with miniature plasma probes made from gold or platinum bond wires

[20], we have been able to demonstrate the first ever OG detection in a microplasma. [18] We have also developed theory to describe how the OG signal is generated in such a system [21]. Still, the spatial distribution of the OG signal in relation to the probes has never been thoroughly investigated, despite the fact that this is a key parameter for both the validation of the theoretical framework, and the evaluation of the technique for LOC. Hence, in this study, the spatial distribution of the OG signal inside the microplasma was investigated in detail. The influence of probe biasing on the distribution was also studied, along with the ability of available theory to explain the observed effects, all in order to evaluate the possibility of using OG spectroscopy as a versatile sensor platform for future LOC sensors. Finally, the stability and sensitivity of the detector was compared with competing techniques for absorption and acoustic spectroscopy.

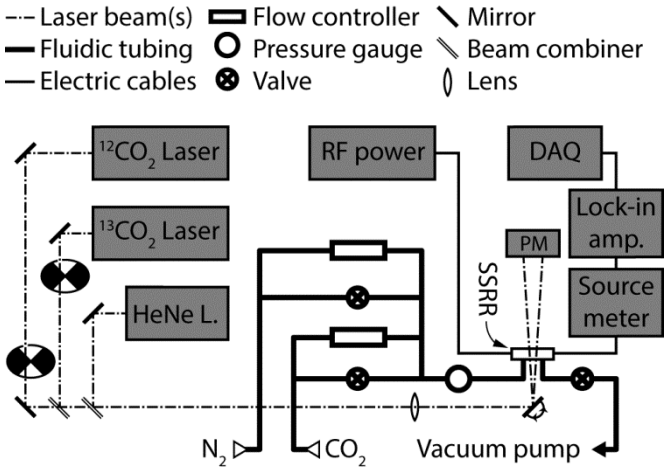

Figure 1. Diagram of the setup with optics, electronics and fluidics**.** The mirror used for scanning the laser beam can be seen at the lower right.

2. Materials and Methods

The setup used in this study consisted of four main sub-systems – optics, fluidics, electronics and, most importantly, the SSRR. A diagram of the system can be seen in figure 1, and specific information on its main components can be found in Appendix A.

The main parts of the optical system were the three lasers – two isotope specific, single-mode CO_2 lasers ($^{12}CO_2$ and $^{13}CO_2$) and a HeNe alignment laser. The beams of the CO_2 lasers were modulated at 40 Hz using optical choppers, before all three beams were parallelized through two iris diaphragms using beam splitters and combiners. The beams were then focused through a ZnSe lens with a focal length of 150 mm, and aligned through the SSRR via a tunable mirror, so that the focal point was centered in the middle of the gap through the SSRR, figure 2. Finally, the laser power(s) were measured using a thermopile power meter. The tuning mirror was equipped with two micrometer screws that could be used to accurately scan the beams across the gap.

The fluidic system allowed for experiments with CO_2, N_2 or mixes of the two, in stationary conditions or at a constant flow rate. During a measurement, the pressure upstream the SSRR was measured by a pressure gauge. The base pressure of the setup was 7 Pa.

The electronics closely resembled those used in Ref. [21], with the only exception that a lock-in amplifier could be connected between the SSRR and the data acquisition (DAQ) to amplify the OG signal. The source meter was used to bias the plasma and measure its I-V characteristics.

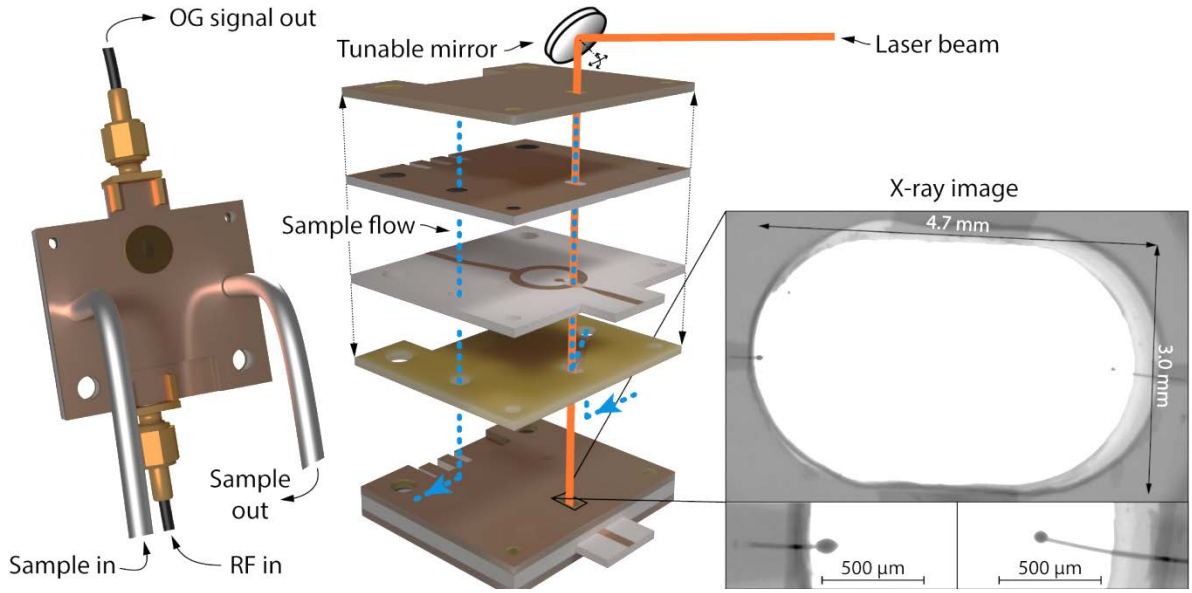

Figure 2. Configuration of the SSRR detector in its present embodiment**.** The middle shows an exploded view of the PCBs of the detector, where the center one incorporates the ring resonator. To the left is an X-ray image of the gap through the SSRR. The two probes can be seen to the left and to the right, and at greater magnification at the bottom. The plasma was generated in the center of the gap.

The SSRR was identical to the one described in Ref. [20], except that the parylene coating of the probes had been removed by plasma etching in an oxygen plasma. It was manufactured by the method described in Ref. [22], and had a resonance frequency of 2.65 GHz, a characteristic impedance of 50 Ω, and the gap through the resonator was 3 mm long and 4.7 mm wide, figure 2, giving the ring an inner and outer radius of 4.49 mm and 6.50 mm, respectively. The gap was sealed by two antireflection coated ZnSe windows, and two ¼ inch steel pipes connected the SSRR to the fluidic system of the setup.

The fused Pt probes [20] of the detector can be seen in figure 2. They were somewhat asymmetric where the left probe was short, 0.20 mm, with a large, ellipsoidal endpoint, whereas the right probe was long, 0.60 mm, with a smaller, spherical endpoint. When ignited, the plasma was not uniformly distributed through the gap, wherefore the probes were subjected to slightly different plasma conditions. The probes could be biased, one at a time, with voltages between -60 V and 60 V using the source meter, while connecting the other to the lock-in amplifier, or directly to the DAQ. The latter is from here on referred to as the active probe. The probes could also be used to study the I-V characteristics of the plasma by scanning the bias voltage while measuring the plasma current with the source meter. From these, the electron temperature could be calculated [19].

The study was based on four principal experiments (Appendix A). In each experiment, the laser beam of the $^{12}CO_2$ laser was stabilized at the P20 transition (λ=10.59 µm), which excited a transition between the first excited vibrational levels the symmetric and asymmetric stretch modes ((100) and (001)) of the $^{12}CO_2$ molecules. The beam was then scanned across the gap though the SSRR while measuring the OG signal, the probe potential, and the laser power. The beam was scanned with 15 horizontal and 17 vertical steps in a rectangular mesh to cover the whole gap. The step length was about 180 µm vertically and 300 µm laterally, and the dwell time was 10 s. The first three experiments studied the OG signal in pure CO_2, flowed through the detector at a rate of 3 sccm. The pressure

upstream the detector was 270 Pa. In the first two experiments the right probe was active while left probe was used to bias the plasma with either 40 V or 60 V. In the third experiment, the left probe was active while the right probe was biased with 40 V, even though this, ideally, would generate identical results as the first experiment. Finally, the fourth experiment was a repetition of the first with the only exception that the CO_2 was replaced by pure N_2.

Some more detailed studies were also performed. The plasmas I-V curve was recorded using the probes as Langmuir probes. These can be found in the Appendix B, and were used to calculate the electron temperature at the position of each probe in the same way as described in Ref. [19]. Moreover, in the experiment where the left probe was biased with 60 V, the stability of the signal was studied by recording a time series of 2000 samples with a sample rate of 1 Hz. Also, spectra of $^{12}CO_2$ and $^{13}CO_2$ were recorded by scanning both CO_2 lasers through their full spectral range (8 lines for the $^{12}CO_2$ laser and 4 lines for the $^{13}CO_2$ laser). Here, the lock-in amplifier was used to improve the signal-to-noise ratio. Finally, the sensitivity of the method was investigated by measuring the OG signal from samples of CO_2 diluted in N_2. These measurements were performed in stationary conditions (no flow) at 300 Pa with CO_2 concentrations of 0, 0.38, 15.6, 226 and 625 ppmv. For each concentration, the electron temperature was measured in the same way as above. The details of all experiments are summarized in Appendix A.

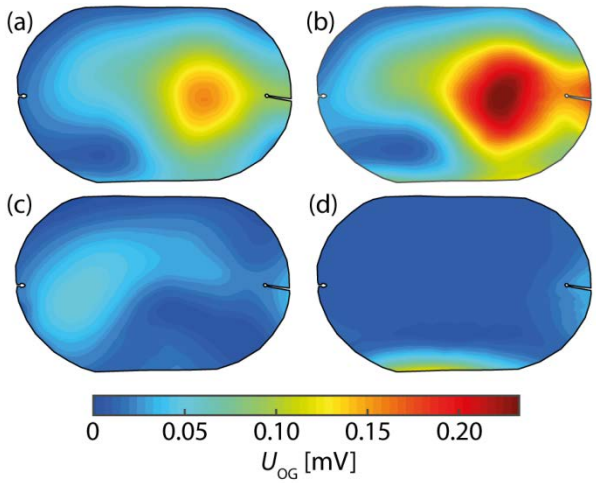

Figure 3. Distribution of the OG signal in the microplasma. In (a), (b) and (c), the sample was pure CO_2, at a pressure and flow rate of 270 Pa and 3 sccm, respectively. In (d), the CO_2 was replaced by N_2 at the same conditions. In (a), (b) and (d), the right probe was used to measure the signal, while the left probe was biased with either 40 V ((a) and (d)) or 60 V (b). In (c), the left probe was used to measure the signal, while the right probe was biased with 40 V. Data points where the laser power had dropped by >50%, from absorption along the edge of the gap, have been excluded and the plot have been cropped with a contour of the gap from figure 2.

3. Results and Discussions

Figure 3 shows the distribution of the OG signal inside the microplasma, after removing thermal interference as described in the Appendix B. The measured signal maxima were displaced to the right if the right probe was active (figure 3(a) and (b)), and to the left if the left probe was active (figure 3(c)), however, only when the detector was filled with CO_2. When instead filled with N_2, no clear OG signal was observed (figure 3(d)). This supported the assumption that the signal was mainly generated inside the sheath of the active probe. Moreover, the amplitude of the OG signal increased with the voltage of the biased probe, although the position of the maxima did not move, i.e., the spatial

distribution remained similar (figures 3(a) and (b)). Most importantly, however, the experiments with pure CO_2 showed significantly different results despite being analyses of the same sample, at identical pressure and flow. Hence, the SSRR detector cannot be used for spectrometry unless these differences can be explained by theory.

In reference 21, it was shown that the OG signal, U_{OG}, in an SSRR detector with double plasma probes can be attributed to a perturbation of the floating potential, U_P, of one of the probes, if the other one is grounded or biased by a constant voltage, U_B. [21] If the electrons in the plasma exhibit a Maxwellian distribution and the pressure, temperature and electric field are at equilibrium, the floating potential is given by the sum of the sheath potential, U_{Sh}, and the plasma potential, U_{PP}, i.e., $U_P = U_{Sh}+U_{PP}$, assuming that $U_{Sh}<0$. [15] On the other hand, if the plasma is subjected to a bias voltage higher than the plasma potential, the sheath around the probe will start to expand, and the floating potential will increase. This increase is linearly dependent on the bias voltage, and will proceed until the dimensions of the sheath become comparable to that of the plasma. At this point the plasma will start to be quenched. [21] The expanding sheath and/or the shifted electron energy and density were probably the reasons for the increased signal amplitude at higher bias voltage.

The perturbation of the floating potential is induced by interactions between the plasma and the laser beam, and since the laser operated in the mid IR regime, where the energy of the photons generally is too low to induce more than rotational or vibrational excitation of the target molecules, the perturbation can be assumed to stem mainly from temperature variations in the different plasma species. [13,21,23] With respect to the floating potential, variations in the electron temperature, $k_B T_e$, will have the greatest influence, since $U_P \sim k_B T_e$. [15] Assuming the perturbations to be small, i.e. $\delta U_P = U_{OG} << U_P$ and $\delta T_e << T_e$, and the bias voltage to be higher than the plasma potential (without quenching it), the OG signal can be approximated by:

$$U_{OG} = n_m I \sigma_L \pi l r^2 \frac{eK_0 U_P}{k_B T_e}, \quad (1)$$

where n_m is the volume density of target molecules, I is the laser power, σ_L is the absorption cross-section of the photon-molecule interaction, $\pi l r^2$ is the irradiated plasma volume, and K_0 is the so called OG proportionality constant. [21]

Hence, using equation (1), it should be possible to normalize the results of figure 3, to correct for the different plasma conditions if the term $n_m \pi l r^2 K_0$ is assumed to be constant in the all experiments studying CO_2. First however, the respective electron temperatures had to be calculated from the plasmas I-V curves, yielding 9.7±0.2 eV in the area around the right probe, and 13.6±0.7 eV around the left. Moreover, the average floating potentials of the active probes were calculated from the scans, yielding 0.7682±0.0005 V and 1.183±0.002 V for right probe biased with 40 V (figure 3(a)) and 60 V (figure 3(b)), respectively, and 0.3808±0.0007 V for the left probe biased with 40 V (figure 3(c)).

Figure 4 shows cross sections of the OG signal from figure 3 along the width of the gap, before and after applying the correction. Before the correction, the measurements showed global signal maxima located in the part of the plasma that was associated with the sheath of the active probe (inset of figure 4). These were properly normalized by the theory (figure 4). However, all three curves also showed local maxima in the part of the plasma that was associated with the sheath of the biased probe. These were not properly normalized by equation (1), probably due to remaining thermal interference, suggesting that the equation is only valid if the laser is aligned to the sheath of the active probe. Still,

in this region, the floating potential could be used to correct for differences in bias voltage, and, combined with the electron temperature, for different plasma conditions. This proves that the mechanism behind the generation of the OG signal can be described by fairly straightforward plasma theory, which is pivotal if the method is to be applied to high-end LOC systems.

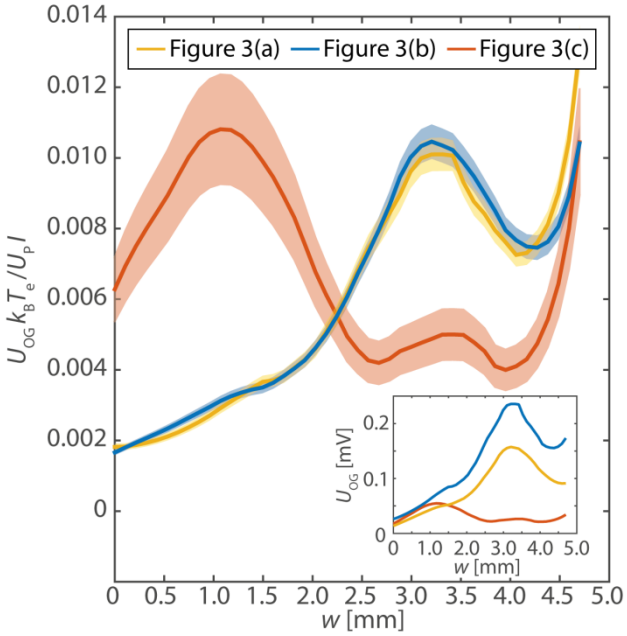

Figure 4. Corrected OG signal. Distribution of the OG signal, U_{OG}, across the length of the gap after correction for the difference in electron temperature, $k_B T_e$, probe potential, U_P, and laser power, I, using equation (1). The shaded boundaries represent a 3σ standard deviation. The inset shows the same data before correction.

The ability of the presented theory to explain the differences between the three experiments implies that the SSRR detector can be used for both spectroscopy and spectrometry as long as both the floating potential and the electron temperature are known. The rather large uncertainty in figure 4 primarily stemmed from uncertainties in the calculation of the electron temperature, wherefore improving this measurement, or finding an alternative, will become desirable in the further application. For example, studying the Thomson scattering of a second laser, e.g., the system's alignment laser, by the free electrons in the plasma could offer a non-perturbing measurement that could be performed continuously and parallel to the OG measurements.

With these results at hand, the obvious question arises: How does miniaturized OG spectroscopy compare with its macroscopic absorption counterpart? Figure 5 shows the overlapping Allan deviation of the setup, where the signal was found to be stable over time spans of up to 140 s. Although it is possible to find absorption spectrometers that are up to one order of magnitude more stable [24], their detectors normally have to be cooled with liquid nitrogen to achieve such performance – something that greatly reduces their integrability in a LOC system. The percent stability of the SSRR detector is similar to an uncooled absorption detector, and there are still room for improvement, since the drift observed in figure 5 mainly stemmed from a drift in the laser wavelength and not in the detector.

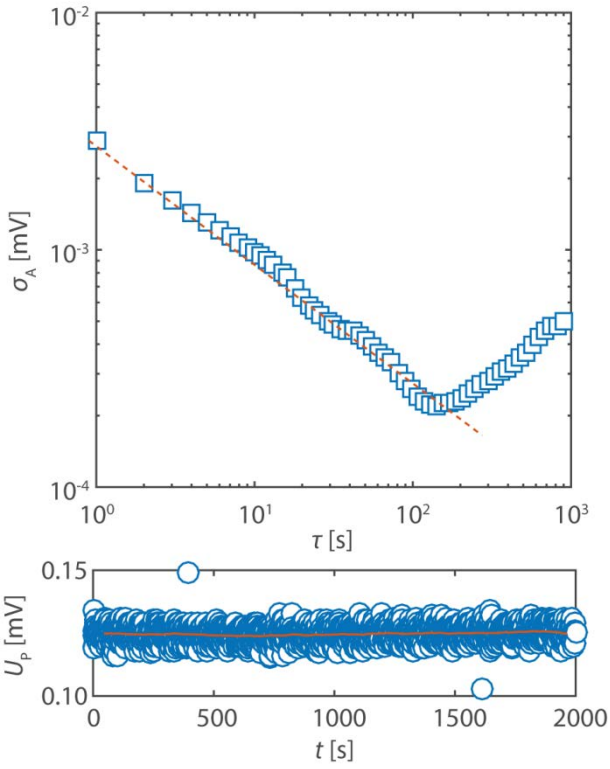

Figure 5. Stability of the OG signal**.** Allan deviation, σ_A, of the setup (top) with the corresponding time series (bottom). The dashed line shows the slope expected for Nyquist and flicker noise, and the solid line shows the time series smoothed with a moving average of 140 s.

With respect to sensitivity, different spectrometers are notoriously difficult to compare [25]. However, two particular figures of merit are often presented – the minimum detectable absorption (MDA) and the noise equivalent absorption sensitivity (NEAS). The MDA is often defined as the lowest absorption signal that can be resolved over the noise floor with 1σ significance at a certain sampling frequency. Hence, the unit of the MDA is $Hz^{-0.5}$, and, commonly, it is given at a sampling frequency of 1 Hz. The NEAS is, in turn, defined as the MDA scaled by the path length, and is a good metric to compare different detectors, since it neglects the influence of the sample cell on the performance of the spectrometer. The value of the NEAS is often given in $cm^{-1}Hz^{-0.5}$.

Figure 6 shows the spectrum of $^{12}CO_2$ and $^{13}CO_2$ when scanning the $^{12}CO_2$ laser, and a second grating-less, single-mode $^{13}CO_2$ laser, through their full spectral ranges (4 and 8 lines for the $^{13}CO_2$ and $^{12}CO_2$ lasers, respectively). As can be seen, clear signals were recorded for both species, even though the total amount of carbon percent inside the 60 µl gap of the SSRR was as low as 80 ng.

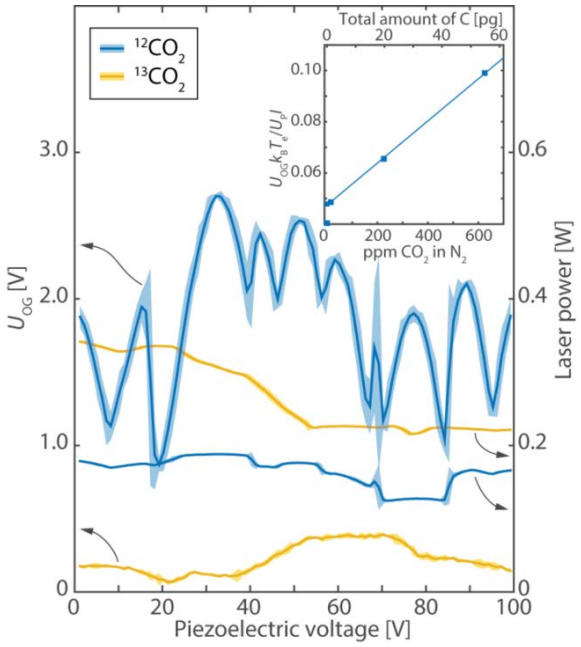

Figure 6. Spectrum of $^{12}CO_2$ and $^{13}CO_2$. Wavelength scans for $^{12}CO_2$ and $^{13}CO_2$ (left y axis), with the respective laser power (right y axis) shown as a reference. The shaded boundaries represent a 3σ standard deviation. The inset shows the scaled OG signal as a function of CO_2 concentration and total amount of carbon.

These isotopic ratio experiments were performed at concentrations far above the LOD of the SSRR detector, as can be seen from the narrow standard deviations in figure 6. To better define the LOD of the detector, the inset of figure 6 shows the OG signal as a function of the CO_2 concentration in an N_2 carrier gas after correction with equation (1). These experiments were conducted in stationary conditions, i.e., without a flow, with a sample frequency of 1 Hz. As can be seen, sub-per mille concentrations, corresponding to only tens of pictograms of carbon, could easily be detected, corresponding to an LOD of less than 100 ppmv. With a more accurate measurement of the electron temperature, and, more importantly, the improved understanding of the spatial distribution of the OG signal gained by this study, we predict that the SSRR detector will be able to reach an LOD below 10 ppmv in a single-pass sample cell.

In order to translate these LOD estimates into values of MDA and NEAS, the absorption inside the gap of the SSRR in the experiments of figure 6, was approximated by simulations in the HITRAN database (http://hitran.iao.ru/). The results are presented in table 1, along with the corresponding input parameters. The gas temperature inside the gap was approximated to 290 K with a flow through the cell and 500 K without[21,26]. The results indicates that the MDA of the SSRR detector is somewhere between $1.4x10^{-10}$ $Hz^{-0.5}$ and $1.4x10^{-9}$ $Hz^{-0.5}$, corresponding to a NEAS between $2.8x10^{-10}$ $cm^{-1}Hz^{-0.5}$and $2.8x10^{-9}$ $cm^{-1}Hz^{-0.5}$.

Table 1. HITRAN simulations of the maximum absorption and absorption coefficient in the experiments presented in figure 6, with corresponding input parameters.

Molecule	Abundance	λ [μm]	p [Pa]	T [K]	Path length [cm]	Absorption	Abs. coef. [cm^{-1}]
$^{13}CO_2$	1.11%	11.15	270	290	0.5	3.7×10^{-6}	7.5×10^{-6}
$^{12}CO_2$	100 ppmv	10.59	300	500	0.5	1.4×10^{-9}	2.8×10^{-9}
$^{12}CO_2$	10 ppmv	10.59	300	500	0.5	1.4×10^{-10}	2.8×10^{-10}

These metrics can now be compared to those of other spectrometric methods, as presented in detail in table 2 and more schematically in figure 7. As can be seen, the detector displays a MDA between one and four orders of magnitude better than most competitors, which must be regarded as exceptional. However, it could be argued that MDA is not a fair way to compare the methods, since most of them benefits from making the sample cell, and hence the path length, longer, while the SSRR detector does not. Hence, a better metric is the single-pass NEAS, where the SSRR detector still outperforms the techniques based on absorption detectors, and is comparable to PAS, should the LOD be reduced towards 10 pmmv.

Table 2. Comparison of the sensitivity of different spectrometers with respect to MDA and NEAS. The latter is given for both single pass (SP) and cavity enhanced (CE) sample cells. *L* corresponds to the length of the sample cell and not the effective path length. All values assume a sample rate of 1 Hz. OA-ICOS refers to off-axis ICOS.

Method	Ref.	MDA [$Hz^{-0.5}$]	*L* [cm]	$NEAS_{SP}$ [$cm^{-1}Hz^{-0.5}$]	$NEAS_{CE}$ [$cm^{-1}Hz^{-0.5}$]
OGS	This work	$<1.4 \times 10^{-9}$	0.5	$<2.8 \times 10^{-9}$	-
CEAS	[2]	2.6×10^{-6}	97.8	2.6×10^{-8}	5.7×10^{-11}
ICOS	[9]	1.7×10^{-4}	0.97	1.8×10^{-4}	6.6×10^{-7}
ICOS	[27]	7.4×10^{-6}	110	6.8×10^{-8}	2.7×10^{-12}
OA-ICOS	[25]	1.0×10^{-5}	90	1.1×10^{-7}	2.4×10^{-11}
OA-ICOS	[3]	1.3×10^{-5}	70	1.9×10^{-7}	3.1×10^{-11}
PAS	[12]	3.9×10^{-9}	9.2	4.3×10^{-10}	-

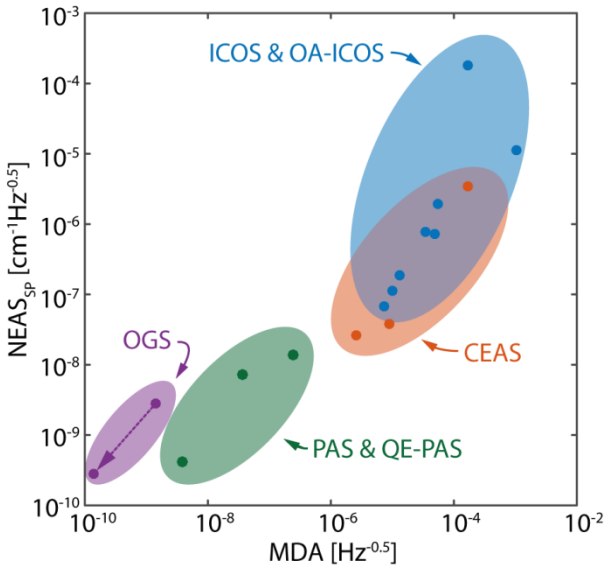

Figure 7. Schematic comparison of the MDA and single-pass NEAS of different spectroscopic techniques at 1 Hz. OA-ICOS refers to off-axis ICOS and QE-PAS to quartz-enhanced PAS. Apart from the data in table 2, values from Refs. [28–35] are included. The purple arrow represents a reduction of LOD from 100 to 10 ppmv.

It could still be said that the absorption detector techniques are more sensitive if the cavity enhancement is taken into account in the calculation of the NEAS. However, the SSRR detector would benefit from cavity enhancement too [36], and table 2 shows that it would only require a cavity with a finesse of ~3100 for it to reach a $NEAS_{CE}$ in the order of 3×10^{-12} $cm^{-1}Hz^{-0.5}$, which must be regarded as reasonable from an engineering point of view.

These experiments confirm that OGS is intrinsically more sensitive than most absorption methods, by up to orders of magnitude, and comparable to PAS in terms of NEAS. However, in LOC applications, OGS must be regarded to outperform PAS too, since the latter requires the sample cell to be pressurized up to atmospheric pressure to be able to deliver maximum performance [12], which is an obvious limitation if the total sample volume is in the order of microliters.

On the topic of LOC, it could also be argued that the SSRR of figure 2 hardly can be regarded as chip-scale. However, the current design of the plasma source is not fully miniaturized, and if chip-level integration is essential, a version made from, e.g., high-temperature co-fired ceramics could be employed [37]. Moreover, the lasers currently used in the setup are quite bulky, and could be replaced by miniature quantum cascade lasers or other IR light sources such as diodes with optical filters ,even though the lasers are commonly not regarded as a part of other laser-based LOC systems, e.g., plasmonic biosensors [38], but rather viewed as auxiliary systems.

4. Conclusions

In conclusion, the spatial distribution of the OG signal in a microplasma has been investigated, revealing a strong signal maximum inside the sheath of the active plasma probe. The signal strength could be increased by biasing an opposing probe with a constant voltage, and the results confirmed the theoretical framework describing the mechanism behind the generation of the signal, which also could be used to calculate the sample concentration. The MDA of the detector was estimated to be less than $1.4\text{x}10^{-9}$ $\text{Hz}^{-0.5}$, which corresponded to a NEAS of $<2.8\text{x}10^{-9}$ $\text{cm}^{-1}\text{Hz}^{-0.5}$. This was at least one order of magnitude better than the detectors used for common cavity enhanced absorption techniques and comparable to detectors for PAS. Given its miniature design, minuscule sample cell volume, high sensitivity, and versatility, the OG detector described in this study shows excellent promise for future LOC gas analyzers, e.g., for $\delta^{13}\text{C}$ measurements in isotope labeling studies of extremely small cell cultures (<1000 cells).

Acknowledgements

Peter Sturesson is acknowledged for his help with the X-ray images. The authors also wish to acknowledge the Swedish National Space Board for supporting the project.

References

[1] Haghighi F, Talebpour Z and Sanati-Nezhad A 2015 Through the years with on-a-chip gas chromatography: a review *Lab Chip*

[2] Landsberg J, Romanini D and Kerstel E 2014 Very high finesse optical-feedback cavity-enhanced absorption spectrometer for low concentration water vapor isotope analyses *Opt. Lett.* **39** 1795–8

[3] Baer D S, Paul J B, Gupta M and O'Keefe A 2002 Sensitive absorption measurements in the near-infrared region using off-axis integrated cavity output spectroscopy *Appl. Phys. B* **75** 261

[4] Raymond P A, Hartmann J, Lauerwald R, Sobek S, McDonald C, Hoover M, Butman D, Striegl R, Mayorga E, Humborg C, Kortelainen P, Durr H, Meybeck M, Ciais P and Guth P 2013 Global carbon dioxide emissions from inland waters *Nature* **503** 355–9

[5] Bastviken D, Tranvik L J, Downing J A, Crill P M and Enrich-Prast A 2011 Freshwater Methane Emissions Offset the Continental Carbon Sink *Sci.* **331** 50

[6] Risby T H and Tittel F K 2010 Current status of midinfrared quantum and interband cascade lasers for clinical breath analysis *Opt. Eng.* **49** 111114–23

[7] Webster C R, Mahaffy P R, Flesch G J, Niles P B, Jones J H, Leshin L A, Atreya S K, Stern J C, Christensen L E, Owen T, Franz H, Pepin R O, Steele A and Team the M S L S 2013 Isotope Ratios of H, C, and O in CO2 and H2O of the Martian Atmosphere *Sci.* **341** 260–3

[8] Leshin L A, Mahaffy P R, Webster C R, Cabane M, Coll P, Conrad P G, Archer P D, Atreya S

K, Brunner A E, Buch A, Eigenbrode J L, Flesch G J, Franz H B, Freissinet C, Glavin D P, McAdam A C, Miller K E, Ming D W, Morris R V, Navarro-González R, Niles P B, Owen T, Pepin R O, Squyres S, Steele A, Stern J C, Summons R E, Sumner D Y, Sutter B, Szopa C, Teinturier S, Trainer M G, Wray J J, Grotzinger J P and Team M S L S 2013 Volatile, Isotope, and Organic Analysis of Martian Fines with the Mars Curiosity Rover *Sci.* **341**

[9] Lou X, Dong Y, Wu D, Wei J and Lu Z 2015 Integrated cavity output spectroscopy by using a sub-centimeter short optical cavity combined with a free-running Fabry–Perot diode laser *Appl. Phys. B* **121** 171–8

[10] Genoud G, Vainio M, Phillips H, Dean J and Merimaa M 2015 Radiocarbon dioxide detection based on cavity ring-down spectroscopy and a quantum cascade laser *Opt. Lett.* **40** 1342–5

[11] Galli I, Bartalini S, Borri S, Cancio P, Mazzotti D, De Natale P and Giusfredi G 2011 Molecular Gas Sensing Below Parts Per Trillion: Radiocarbon-Dioxide Optical Detection *Phys. Rev. Lett.* **107** 270802

[12] Pushkarsky M B, Webber M E and Patel C K N 2003 Ultra-sensitive ambient ammonia detection using CO2-laser-based photoacoustic spectroscopy *Appl. Phys. B* **77** 381–5

[13] Barbieri B, Beverini N and Sasso A 1990 Optogalvanic spectroscopy *Rev. Mod. Phys.* **62** 603–44

[14] Walkup R, Dreyfus R W and Avouris P 1983 Laser Optogalvanic Detection of Molecular Ions *Phys. Rev. Lett.* **50** 1846–9

[15] Suzuki T, Sekiguchi H and Kasuya T 1983 OPTOGALVANIC DETECTION WITH MICROWAVE DISCHARGE *J. Phys. Colloq.* **44** C7–419 – C7–427

[16] Schneck P K and Hastie J W 1981 Optogalvanic Spectroscopy-Application To Combustion Systems *Opt. Eng.* **20** 204522–204522 –

[17] Berthoud T, Lipinsky J, Camus P and Stehle J L 1983 Electron pulse shape in laser-enhanced ionization spectrometry *Anal. Chem.* **55** 959–63

[18] Berglund M, Thornell G and Persson A 2013 Microplasma source for optogalvanic spectroscopy of nanogram samples *J. Appl. Phys.* **114** 33302

[19] Berglund M, Grudén M, Thornell G and Persson A 2013 Evaluation of a microplasma source based on a stripline split-ring resonator *Plasma Sources Sci. Technol.* **22** 55017

[20] Berglund M, Sturesson P, Thornell G and Persson A 2015 Manufacturing miniature Langmuir probes by fusing platinum bond wires *J. Micromechanics Microengineering* **25** 105012

[21] Persson A, Berglund M and Salehpour M 2014 Improved optogalvanic detection with voltage biased Langmuir probes *J. Appl. Phys.* **116** 243301

[22] Persson A, Berglund M, Thornell G, Possnert G and Salehpour M 2014 Stripline split-ring resonator with integrated optogalvanic sample cell *Laser Phys. Lett.* **11** 45701

[23] Webster C R and Menzies R T 1983 Infrared laser optogalvanic spectroscopy of molecules *J. Chem. Phys.* **78**

[24] van Helden J H, Lang N, Macherius U, Zimmermann H and Röpcke J 2013 Sensitive trace gas detection with cavity enhanced absorption spectroscopy using a continuous wave external-cavity quantum cascade laser *Appl. Phys. Lett.* **103** -

[25] Moyer E J, Sayres D S, Engel G S, St. Clair J M, Keutsch F N, Allen N T, Kroll J H and Anderson J G 2008 Design considerations in high-sensitivity off-axis integrated cavity output spectroscopy *Appl. Phys. B* **92** 467–74

[26] Eilers G, Persson A, Gustavsson C, Ryderfors L, Mukhtar E, Possnert G and Salehpour M 2013 The radiocarbon intracavity optogalvanic spectroscopy setup at Uppsala *Radiocarbon* **55**

[27] Engel G S, Drisdell W S, Keutsch F N, Moyer E J and Anderson J G 2006 Ultrasensitive near-infrared integrated cavity output spectroscopy technique for detection of CO at 1.57 μm: new sensitivity limits for absorption measurements in passive optical cavities *Appl. Opt.* **45** 9221–9

[28] Zhao W, Gao X, Chen W, Zhang W, Huang T, Wu T and Cha H 2006 Wavelength modulated off-axis integrated cavity output spectroscopy in the near infrared *Appl. Phys. B* **86** 353–9

[29] Malara P, Maddaloni P, Gagliardi G and De Natale P 2006 Combining a difference-frequency source with an off-axis high-finesse cavity for trace-gas monitoring around 3 μm *Opt. Express* **14** 1304–13

[30] Bakhirkin Y A, Kosterev A A, Curl R F, Tittel F K, Yarekha D A, Hvozdara L, Giovannini M and Faist J 2005 Sub-ppbv nitric oxide concentration measurements using cw

thermoelectrically cooled quantum cascade laser-based integrated cavity output spectroscopy *Appl. Phys. B* **82** 149–54
[31] Paul J B, Lapson L and Anderson J G 2001 Ultrasensitive absorption spectroscopy with a high-finesse optical cavity and off-axis alignment *Appl. Opt.* **40** 4904–10
[32] Bayrakli I and Akman H 2015 Ultrasensitive, real-time analysis of biomarkers in breath using tunable external cavity laser and off-axis cavity-enhanced absorption spectroscopy *J. Biomed. Opt.* **20** 37001
[33] Kosterev A A and Tittel F K 2004 Ammonia detection by use of quartz-enhanced photoacoustic spectroscopy with a near-IR telecommunication diode laser *Appl. Opt.* **43** 6213–7
[34] Bernhardt B, Ozawa A, Jacquet P, Jacquey M, Kobayashi Y, Udem T, Holzwarth R, Guelachvili G, Hansch T W and Picque N 2010 Cavity-enhanced dual-comb spectroscopy *Nat Phot.* **4** 55–7
[35] Borri S, Patimisco P, Galli I, Mazzotti D, Giusfredi G, Akikusa N, Yamanishi M, Scamarcio G, De Natale P and Spagnolo V 2014 Intracavity quartz-enhanced photoacoustic sensor *Appl. Phys. Lett.* **104**
[36] Persson A and Salehpour M 2015 Intracavity optogalvanic spectroscopy: Is there any evidence of a radiocarbon signal? *Nucl. Instruments Methods Phys. Res. Sect. B Beam Interact. with Mater. Atoms*
[37] Berglund M, Persson A and Thornell G 2015 Evaluation of dielectric properties of HTCC alumina for realization of plasma sources *J. Electron. Mater.* **44** 3654–60
[38] Estevez M-C, Otte M A, Sepulveda B and Lechuga L M 2014 Trends and challenges of refractometric nanoplasmonic biosensors: A review *Anal. Chim. Acta* **806** 55–73

Appendix A. Measurement setup

Figure 1 shows the schematics of the setup used in this study. Its function is more thoroughly described in the Methods section, and the details of the different components can be found in table A1. Table A2 summarizes the details of the different experiments based on in which figure in the manuscript they are presented.

Table A1. Most important components of the setup.

Component	Name	Manufacturer	Location
$^{12}CO_2$ laser	Merit-SL	Access Laser Co.	Everett, WA, USA
$^{13}CO_2$ laser	L20-SZ	Access Laser Co.	Everett, WA, USA
HeNe laser	CPS-180	Anteryon	Eindhoven, The Netherlands
Beam splitter	BS7-1-350%R-PIS	Wavelength Technology Singapore Ltd.	Singapore
Beam combiner	102 BS3-GS-R	Wavelength Technology Singapore Ltd.	Singapore
$^{12}CO_2$ laser chopper	Model SR540	Stanford Research Systems	Sunnyvale, CA, USA
$^{13}CO_2$ laser chopper	MC2000 Optical Chopper	Thorlabs Inc.	Newton, NJ, USA
Computer	Z230 Workstation	Hewlett Packard	Palo Alto, CA, USA
Data acquisition	PCI 6120 with a BNC-2110 connector block	National Instruments Corp.	Austin, TX, USA
Lock-in amplifier	SR530	Stanford Research Systems	Sunnyvale, CA, USA
CO_2 gas	CO_2 N40	Air Liquide	Paris, France
N_2 gas	Internal laboratory supply system	-	-
Lens	LA7028-F	Thorlabs Inc.	Newton, NJ, USA
Mirrors	PF10-03-P01	Thorlabs Inc.	Newton, NJ, USA
Windows	WG70530-F	Thorlabs Inc.	Newton, NJ, USA
Tuning mirror	Slimline Gimbal Mount 19295	Oriel	Darmstadt, Germany
Power meter	S310C	Thorlabs Inc.	Newton, NJ, USA
Pipes and tubing	¼ inch steel pipes	Swagelok	Solon, USA
Pressure gauge	275 Mini-Converter	Brooks Automation Inc.	Chelmsford, MA, USA
Source meter	Model 2400	Keithley Instruments Inc.	Cleveland , OH, USA
Vacuum pump	AMM712/A4R3	Pfeiffer Vacuum AG	Asslar, Germany

Table B2. Details of the main experiments. The probe numbering refers to figure 2.

Experiment	Biased probe	U_B [V]	Gas	p [Pa]	f_C [Hz]	Flow [sccm]	*Ampl.*
Figures 3(a), 4 and B2(a)	Left	40	CO_2	270	40	3	Non
Figures 3(b), 4 and B2(b)	Left	60	CO_2	270	40	3	Non
Figures 3(c), 4 and B2(c)	Right	40	CO_2	270	40	3	Non
Figures 3(d) and B2(d)	Left	40	N_2	270	40	3	Non
Figure 5	Left	60	CO_2	270	40	3	Non
Figure 6	Left	60	CO_2	270	40	3	Lock-in
Figure 6 (inset)	Left	60	CO_2 in N_2	300	40	0	Non
Figure S3	Left/Right	-60 to 60	CO_2	270	40	3	Non

Appendix B. Thermal interference & I-V curves

Figure B1 shows the results of scanning the laser beam of the $^{12}CO_2$ laser across the gap through the SSRR. As can be seen, the gap served as diaphragm for the laser beam, where the distribution of the measured laser power accurately depicted the geometry of the gap. Based on this observation, an outline of the gap from figure 2 was fitted to the spatial scans, approximately along the contour line where the laser power had halved, in order to show the approximate positions of the probes in both figures 3 and B1. Moreover, directing the laser beam below the gap generated a strong signal in the OG measurement. However, the origin of this signal was most likely not optogalvanic, since 1.) It was generated without transmitting light through the gap, and 2.) It was still visible in the experiment where the CO_2 sample had been replaced by pure N_2 (figure B1 (d)). Instead, the origin of this signal was probably thermal[20], where its asymmetry can be explained by the SSRR being slightly tilted with respect to the laser beam, allowing it to hit the lower wall of the gap. For the same reasons, the strong signal observed around the right probe in figure B1 (a), (b) and (d) was most likely thermal in origin too, and caused by the direct illumination of the probe by the laser beam. The reason why no such effect was observed in figure B1(c) was probably the much shorter length of the left probe, protecting it from direct illumination. Finally, a less intense signal was observed inside the volume of the gap if it was filled with CO_2 (figure B1(a), (b) and (c), but not if it was filled with N_2 (figure B1(d)). Hence, this signal was interpreted as being optogalvanic in origin.

In order to distinguish the OG signal from the thermal interference, particularly that caused by the direct illumination of the probes, figure 3 was post processed and shows two-dimensional quadratic, locally weighted scatterplot fits to the data from figure B1, where the area around the right probe was excluded together with points where the laser power had halved. Still, some thermal interference remained around the right probe and in the lower part of the gap, particularly in figure 3(d). However, the post processing made the OG signal become the dominant effect, and figure 3 useful for interpreting the spatial distribution of the OG effect in the microplasma.

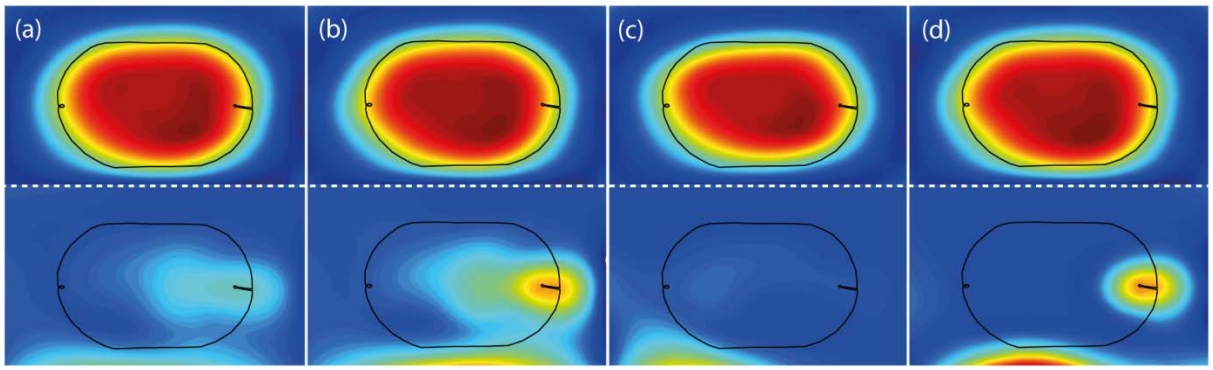

Figure B1. Spatial distribution of the laser power (top) and OG signal (bottom) when scanning the laser beam across the gap. In (a), (b) and (c), the sample was pure CO_2, at a pressure and flow rate of 270 Pa and 30 sccm, respectively. In (d), the CO_2 was replaced by N_2 at the same conditions. In (a), (b) and (d), the right probe was used to measure the signal, while the left probe was biased with either 40 V ((a) and (d)) or 60 V (b). In (c), the left probe was used to measure the signal, while the right probe was biased with 40 V. The images are contour plots with 100 levels of quadratic, locally weighted scatterplot fits (span=25%). The top and bottom color maps are linear between 0 and 201 mW and 0 and 0.87 mV, respectively. The lines are aligned contours of the gap from figure 2.

Figure B2 shows the plasma's I-V curves that were used for calculating the electron temperature of the plasma in the volume around the two probes. These calculations were made in the same way as in references 21 and 22, by assuming collisionless, un-magnetized plasma conditions

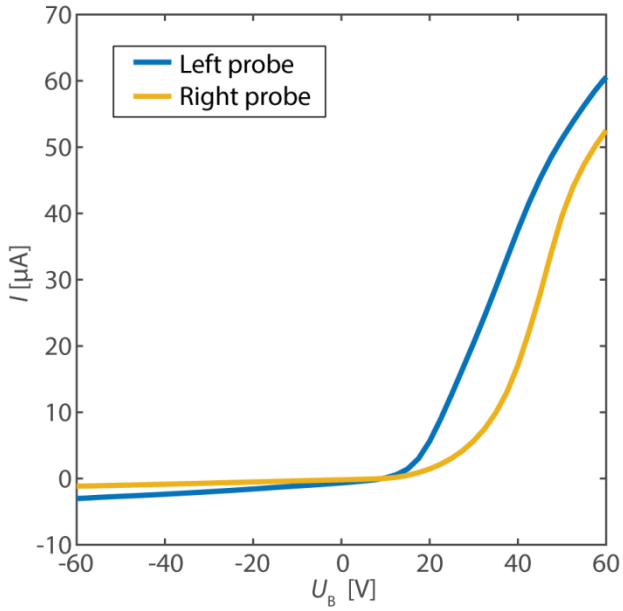

Figure B2. I-V curves of the two probes from which the electron temperatures were calculated.